I&EC research
Industrial & Engineering Chemistry Research

Article

pubs.acs.org/IECR

Scale-up of Nanoparticle Synthesis by Flame Spray Pyrolysis: The High-Temperature Particle Residence Time

Arto J. Gröhn,[†] Sotiris E. Pratsinis,[†] Antoni Sánchez-Ferrer,[‡] Raffaele Mezzenga,[‡] and Karsten Wegner*[,†]

[†]Particle Technology Laboratory, Department of Mechanical and Process Engineering, Swiss Federal Institute of Technology (ETH) Zurich, Sonneggstrasse 3, CH-8092 Zurich, Switzerland

[‡]Laboratory of Food and Soft Materials, Department of Health Sciences and Technology, Swiss Federal Institute of Technology (ETH) Zurich, Schmelzbergstrasse 9, CH-8092 Zurich, Switzerland

Supporting Information

ABSTRACT: The scale-up of nanoparticle synthesis by a versatile flame aerosol technology (flame spray pyrolysis) is investigated numerically and experimentally for production of ZrO_2. A three-dimensional computational fluid dynamics model is developed accounting for combustion and particle dynamics by an Eulerian continuum approach coupled with Lagrangian description of multicomponent spray droplet atomization, transport, and evaporation. The model allows the extraction of the high-temperature particle residence time (HTPRT) that is governed by the dispersion gas to precursor liquid mass flow ratio as well as the flame enthalpy content. The HTPRT is shown to control the primary particle and agglomerate size, morphology, and even ZrO_2 crystallinity in agreement with experimental data. When the HTPRT is kept constant, the production rate for ZrO_2 nanoparticles could be scaled up from ~100 to 500 g/h without significantly affecting product particle properties, revealing the HTPRT as a key design parameter for flame aerosol processes.

1. INTRODUCTION

One of the most promising methods for cost- and material-effective manufacture of nanoparticles is flame aerosol technology.[1,2] To date, however, only a few basic oxides and carbon black are produced industrially (tons per day) by this technique,[3] attributed to the limited choice of low-cost volatile raw materials. Flame spray pyrolysis (FSP)[4] that is already used for industrial manufacture of carbon black[5] or specialty chemicals such as functionalized cobalt nanoparticles[6,7] has the potential to change this picture as it allows synthesis of multicomponent nanoparticles of almost all elements from relatively inexpensive liquid or solid precursors and solvents.[8] Compared to "ideal" vapor-fed premixed flames, FSP has the additional complexity of droplet formation and precursor release leading to solid or hollow particles. This challenge is not present in the design of commercial vapor-fed flame reactors prompting a fundamental investigation to connect such product characteristics to process variables based on sound engineering principles and models.[9]

While synthesis of numerous nanomaterials for various applications has been demonstrated with laboratory FSP reactors,[10] only a few compositions have been made at pilot-scale (>100 g/h), such as CeO_2/ZrO_2,[11] SiO_2,[12] ZrO_2,[13] Y_2O_3/ZrO_2,[14] $La_{0.6}Sr_{0.4}Co_{0.2}Fe_{0.8}O_{3-\delta}$,[15] $FePO_4$,[8] and ZnO.[16] No systematic scale-up studies have been carried out to advance nanoparticle manufacture by FSP. In such a scale-up, the production rate should be increased from grams per hour to several kilograms per hour without affecting nanoparticle characteristics. In flame aerosol synthesis, product particle size and structure are controlled by the high-temperature particle residence time (HTPRT) and concentration through the particle sintering and coagulation rates.[17] For example, in FSP, increasing the production rate by increasing the precursor flow yields larger flames and longer HTPRT, prolonging particle sintering or coalescence that results in larger primary particles.[12] In contrast, higher dispersion gas flow decreases product primary particle diameters by diluting the flame and decreasing the high-temperature residence time.[13,18]

For aerosol reactor scale-up of coaxial jet diffusion flames, Sadakata et al.[19] suggested that the ratio of burner tube diameter to reactant outlet velocity must be kept constant. Mädler et al.[20] showed for a lab-scale FSP reactor that a constant dispersion gas to precursor flow ratio resulted in similar primary particle size of ceria during production rate increase from 2 to 10 g/h. Wegner and Pratsinis[3,21] showed that for a given material and production rate, constant particle size was attained by maintaining the difference of reactant outlet velocities in three diffusion flame reactors for production of silica and titania nanoparticles of the same size and morphology up to 200 g/h.

Here, scale-up of the FSP process is investigated by computational fluid dynamics (CFD) and detailed experimentation in a pilot-scale reactor by the example of zirconia synthesis from 100 to 500 g/h. Therefore, a two-dimensional model[18] is extended to account for droplet breakup and the three-dimensional reactor geometry. Model predictions are compared to measured primary and agglomerate particle characteristics, exploring the application of the HTPRT as a process design parameter for the scale-up of FSP.

Received: April 25, 2014
Revised: June 10, 2014
Accepted: June 11, 2014
Published: June 11, 2014

dx.doi.org/10.1021/ie501709s | Ind. Eng. Chem. Res. 2014, 53, 10734−10742

2. EXPERIMENTAL SECTION

2.1. Set-up. Figure 1a shows the FSP burner head consisting of a two-phase atomizer nozzle (based on Düsen-

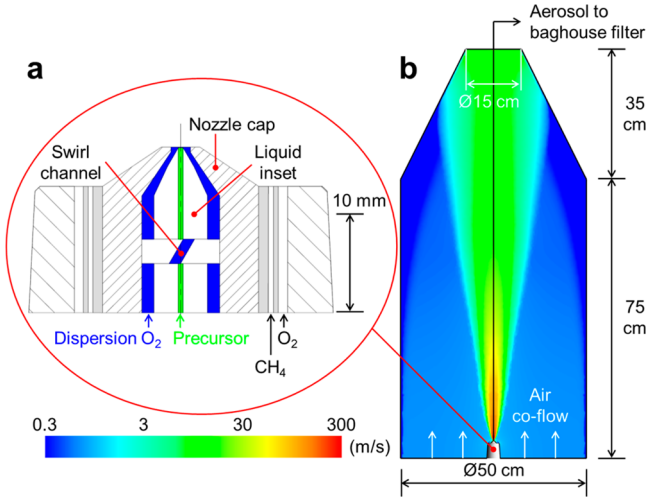

Figure 1. (a) Schematic of the FSP two-phase atomizer geometry. The liquid precursor is delivered through the center capillary, dispersed with oxygen, and ignited by a methane/oxygen pilot flame. (b) The FSP reactor is centered in the cylindrical reactor chamber and surrounded by a homogenized coflow of ambient air that satisfies the entrainment requirement of the spray flame and cools the aerosol before collection with a bag-house filter. Velocity contours for the largest spray flame burning 64 mL/min of precursor solution dispersed by 80 L/min of O_2 indicate that no recirculation zones are present in the reactor.

Schlick, Model 970) and surrounding channels for a coflow diffusion pilot flame. The liquid precursor is delivered through the central insert with a 0.5 mm (i.d.) capillary. A cap with 2.6 mm bore surrounds this insert, forming a gap for the oxygen dispersion gas. Eight 0.5 mm wide channels 0.9 cm below the nozzle outlet are arranged at a 30° angle imposing swirl on the dispersion gas. Moving the liquid insert up or down controls the width of the dispersion gas outlet gap and consequently its pressure drop, which is set here to ~3.5 bar independent of oxygen flow.

A 1 mol/L Zr precursor solution (Table 1) made from zirconium 2-ethylhexanoate (Valirex 18 wt % Zr, Umicore; here abbreviated as Zr-EHA) and xylenes (Thommen-Furler, 253-VL51TE) was delivered with a syringe pump (Teledyne ISCO, D1000) to the water-cooled nozzle capillary at 16−64 mL/min, corresponding to 118−472 g/h ZrO_2 production rate. That solution was atomized with 20−80 L/min of oxygen (99.95%, PanGas) forming a spray that was ignited by the surrounding diffusion flame of 2.0 L/min methane (99.5%, PanGas; inner burner channel, 1.8 cm i.d., 0.5 mm gap) and 4.5 L/min oxygen (99.95%, PanGas; outer burner channel, 2.0 cm i.d., 1 mm gap). All gas flows are reported at 273.15 K and 1.013×10^5 Pa and were kept constant by mass flow controllers. Here, the flames are termed as X/Y flames with X being the precursor flow rate in milliliters per minute and Y the dispersion O_2 flow rate in liters per minute.

The FSP reactor was centered at the bottom of a cylindrical 50 cm i.d. stainless steel chamber of 1.1 m height that narrowed down to 15 cm i.d. at 75 cm (Figure 1b). A homogenized coflow of ambient air (~8300 L/min) was established with a centrifugal fan to minimize recirculation by satisfying the

Table 1. Boundary Conditions of the CFD Simulations (Zr-EHA = Zirconium-2-ethylhexanoate)

boundary		type	mass flow (g/s) or (pressure (Pa))	composition (wt %)
liquid capillary (precursor solution)	Zr: 0 M	droplet injection	0.23−0.92	xylenes: 100
	Zr: 1 M		0.26−1.05	Zr-EHA: 52; xylenes: 48
pilot flame channel		mass flow inlet	2.39×10^{-2}	CH_4: 100
			1.07×10^{-1}	O_2: 100
dispersion oxygen slit		mass flow inlet	0.48−1.90	O_2: 100
sheath gas		pressure inlet	(101325)	O_2: 23; N_2: 77
outlet		pressure outlet	1.67×10^2	–
burner/reactor walls		wall no-slip	–	–

entrainment requirements of the enclosed spray flame[22] and to dilute and cool the aerosol before nanoparticles were collected with a bag-house filter. Particle samples were extracted by a vacuum pump 1.2 m downstream the reactor chamber on glass fiber filters (Albet-Hahnemühle, GF 6, Ø 25.7 cm) placed in a stainless steel filter holder.

The specific surface area (SSA) of product zirconia nanoparticles was determined by nitrogen adsorption at 77 K (Micromeritics Tristar 3000) after degassing in nitrogen at 200 °C for at least 1 h. The primary particle diameter was calculated as $d_p = 6/(\rho_p \text{ SSA})$ assuming monodisperse spheres (BET-equivalent diameter) and employing a density of $\rho_p = 5.72 \times 10^3$ kg/m^3 for tetragonal zirconia.[23] The powder crystallinity was determined by X-ray diffraction (XRD; Bruker D8 Advance, 40 kV, 40 mA, Cu Kα radiation, Bragg−Brentano geometry) in the range of $2\theta = 20-70°$. The XRD patterns were analyzed using Topas 4.2 software (Bruker AXS). Phase composition and crystal sizes were obtained by Rietveld refinement. A first-order Chebychev function was used for background correction.

The morphology of product particles was determined by transmission electron microscopy (TEM, Tecnai F30 ST). Therefore, agglomerates scraped off the sampling filter were dispersed in ethanol and applied to TEM grids. Powders were also analyzed by small-angle X-ray scattering (SAXS) using a Rigaku (MicroMax-002+) X-ray source with microfocused beam (40 W, 45 kV, 0.88 mA, Cu Kα radiation) which was collimated by three pinhole (0.4, 0.3, and 0.8 mm) collimators. The scattered X-ray intensity was detected with a two-dimensional Triton-200 X-ray gas-filled detector (20 cm diameter, 200 μm resolution). An effective scattering vector range of 0.005−0.2 Å^{-1} was obtained. An empirical multiple level unified exponential/power-law method was used for fitting of the SAXS scattering spectra.[24,25]

2.2. Spray Flame Temperature Measurements. Temperature profiles of particle-free burning spray flames were characterized outside the reactor chamber in stagnant ambient air using pure xylenes as fuel and otherwise identical conditions as in the particle synthesis experiments. The standard combustion enthalpy of xylenes ($\Delta H°_C = 3.7 \times 10^4$ kJ/L)[26] is close to that of the 1 M Zr precursor solution ($\Delta H°_C = 3.4 \times 10^4$ kJ/L) where the Zr-EHA (described as zirconium(IV)

dx.doi.org/10.1021/ie501709s | Ind. Eng. Chem. Res. 2014, 53, 10734−10742

hydride 2-ethylhexanoate, $ZrH(C_8H_{15}O_2)_3$) is approximated by three $C_8H_{16}O_2$ molecules ($\Delta H°_C = 3.0 \times 10^4$ kJ/L).[27] The line-of-sight flame temperature was measured by Fourier-transform infrared spectroscopy (FTIR, Bomem MB 155S, deuterated triglycine sulfate detector, wavenumber range 6500−500 cm^{-1}, resolution 32 cm^{-1}) by fitting a blackbody Planck function through the measured hot CO_2 radiance spectra.[28,29] A 1 cm diameter IR beam was used to increase the signal-to-noise ratio.[18] Up to 2048, 1024, and 128 scans were taken at 1−50 cm HAB for transmission, emission, and background spectra, respectively.

3. THEORY

The entire FSP reactor chamber along with detailed nozzle geometry (Figure 1) was implemented as a three-dimensional computational grid. The domain was represented by a 90° segment (~1 000 000 cells) with periodic boundary conditions due to symmetry. The inlet temperature of all fluids was set to 300 K, and the walls were considered thermal insulators. Details on boundary conditions and model equations are summarized in Table 1 and Supporting Information, respectively. Computational fluid dynamic (CFD) simulations were carried out with the pressure-based, coupled steady-state solver of ANSYS Fluent v.12.1.4 accounting for heat transport but neglecting radiation.[30]

Turbulent flow was modeled with the realizable k-ε model.[31] All variables were solved with second-order spatial discretization,[30] while the PRESTO! algorithm[32] was applied for pressure interpolation. Gravity was included to account for buoyancy. The present approach combined with the complete reactor geometry allows the definition of all boundary and process conditions by mass flow rates and compositions, as in the experiments, without relying on correlations for initial droplet size and dispersion gas velocity.[18]

The liquid injection is described by discrete parcels ("blobs") with 0.5 mm diameter and 1.36−5.43 m/s velocity defined by the liquid capillary size and mass flow,[33] assuming that atomization and subsequent droplet breakup are indistinguishable processes within the dense near nozzle spray. The lamella-to-droplet breakup is described by the Wave model[34] appropriate for high Weber numbers (We >100). The Kelvin−Helmholtz instability is assumed to be the dominant breakup mechanism (here, We >1000 near nozzle).[30]

The characteristic breakup time is given as $\tau_b = (1.863 B_1 d_d)/(\Omega_w \Lambda)$, where d_d is the droplet diameter. The maximum growth rate of the unstable wave (Ω_w) and the corresponding wavelength (Λ) are obtained from curve fits to numerical solutions of the dispersion relation.[30] The breakup constant (B_1) was set to ten[34] allowing for the Wave model to approach[35] the semiempirical Pilch−Erdman correlations.[36] This method can predict droplet size distributions and therefore size-dependent droplet trajectories.

A dynamic drag model[37] was applied to account for droplet distortion and oscillation at the present high-Weber number conditions. The relative motion between droplet and gas phases causes the drag to vary between that of a sphere and a disk at limits of zero and maximum distortion.[30] An iteration time step of 10^{-7} s was used for the unsteady Lagrangian particle tracking to solve the mass, enthalpy, and momentum balance equations for the liquid and gas phase.[18]

Gas-phase oxidation reactions were limited either by mass transport[38] or one-step global Arrhenius kinetics,[39,40] and the lower (limiting) rate at each computational cell was employed. The precursor was described as $ZrH(C_8H_{15}O_2)_3$ molecules. Its oxidation taking place above 1000 K was assumed to be limited by mass transport only.[18]

$$\text{Zr-EHA:}\quad 2ZrH(C_8H_{15}O_2)_3 + 67O_2 = 2ZrO_2 + 48CO_2 + 46H_2O$$

$$\text{xylene:}\quad 2C_8H_{10} + 21O_2 = 16CO_2 + 10H_2O$$

$$\text{methane:}\quad CH_4 + 2O_2 = CO_2 + 2H_2O$$

The evolution of particle volume, area, and number concentration was simulated with the CFD solver accounting for nucleation, coagulation, and sintering.[41] A monodisperse model[42] was employed as the self-preserving particle size distribution is rapidly attained[43] for flame-made ZrO_2.[44] The particle nucleation rate was assumed to be identical to the precursor oxidation rate on a mass basis. Possible errors in critical cluster size for nucleation become negligible because of rapid coagulation.[45] The coagulation rate was computed using a fractal-like dimension of 1.8, typical for diffusion-limited cluster−cluster agglomeration.[46] Sintering kinetics of zirconia according to Coblenz et al.,[47] Brossmann et al.,[48] and Christensen and Carter[49] were selected among others based on comparison of lab-scale FSP model predictions to measured ZrO_2 primary particle diameters.[18]

4. RESULTS AND DISCUSSION

4.1. Spray Combustion Temperature. Figure 1b shows velocity contours of the largest spray flame (burning 64 mL/min of precursor solution dispersed by 80 L/min of O_2, a 64/80 flame) indicating that (a) the reactor chamber does not interfere with the free jet expansion in ~1 m/s air coflow and (b) recirculation zones are not formed. Flame diagnostics carried out without the chamber in stagnant air are thus considered to adequately represent the enclosed system.

Spray flame temperatures were investigated in the absence of ZrO_2 particle formation by combustion of 16, 32, or 64 mL/min of xylenes dispersed by 20, 40, or 80 L/min of O_2 (16/20, 32/40, 64/80 and 16/80 flames, respectively). Simulated (lines) and FTIR-measured (symbols) line-of-sight average temperature profiles between HAB = 0 and 50 cm are shown in Figure 2. Model predictions are also line-of-sight averages to be consistent with the CO_2 molar concentration weighed measurements.

The highest temperatures of ~3730 ± 30 K, ~3300 ± 110 K, and ~3730 ± 260 K were obtained at HAB = 1−3 cm for the 16/20, 32/40, and 64/80 flames, respectively. The 64/80 flame temperature stayed close to ~3500 ± 500 K up to HAB = 10 cm before it decreased to 940 K at 50 cm HAB. For both 32/40 and 16/20 flames, the temperature decreased to 2300 K at HAB = 10 cm and further to ~1000 K at 30 cm. The 16/80 flame was significantly colder with a maximum of 1850 K at HAB = 3 cm and 700 K at 20 cm. For that flame, measuring at HAB = 1 cm was not possible because of high noise level.

Simulations of the 32/40 and 64/80 flames predicted a comparable temperature maximum of ~3500 K slightly downstream at 4 cm HAB but lower maximum temperatures of ~3000 and ~2000 K for the 16/20 and 16/80 flames, respectively. The model underpredicted the measurement averages of the 64/80 flame at 10 and 20 cm HAB by ~750 and 670 K, respectively, while excellent agreement was obtained for larger heights. Similar results were observed for other flame conditions where measurements were underpredicted by up to ~700 K below 10 cm HAB while higher up temperatures

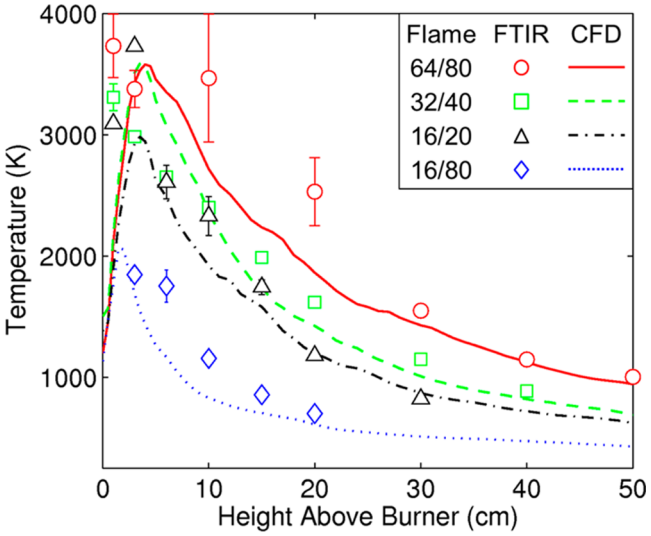

Figure 2. CFD predicted (lines) and FTIR measured (symbols) line-of-sight axial temperature profiles for spray combustion of 16 (triangles, dash-dotted line), 32 (squares, dashed line), and 64 mL/min (circles, solid line) of xylenes dispersed by 20, 40, and 80 L/min of O_2, respectively. Also shown is the 16/80 flame (diamonds, dotted line). Good agreement between measurements and simulations is obtained especially downstream of the spray region with low signal-to-noise ratios and high radial gradients.

agreed within ~250 K, attributed to improved signal-to-noise ratio and thus smaller measurement error.

Similar to laboratory-scale FSP,[18,50] combustion commences close to the burner where fuel droplets and dispersion oxygen are intensely mixed and ignited by the supporting methane–oxygen flame. Here, simulated and measured temperatures decrease above HAB = 5 cm, indicating that by then most of the fuel is consumed while air entrainment further cools the flame downstream.[22] Higher FTIR-measured temperatures at HAB = 1 cm may be attributed to underestimated gas-phase reaction rates in the CFD model. Differences could also be caused by the difficulty of comparing the CO_2-weighed line-of-sight average temperatures at conditions where steep radial temperature gradients are present.[41]

Previously, for burning sprays of either pure ethanol[18] or zirconium(IV) *n*-propoxide dissolved in ethanol,[44] the highest measured temperatures were ~3000 and ~2750 K, respectively, compared to ~3700 K here for xylenes. These differences are caused by the lower adiabatic flame temperature of stoichiometric ethanol combustion in oxygen (~3000 K) compared to that of xylenes (~3200 K). Both measured and simulated maximum temperatures here are higher than the adiabatic flame temperature for xylenes/oxygen. While the maximum temperature in simulations may be overestimated by the employed one-step global oxidation chemistry, the measured temperatures may indicate nonequilibrium concentrations of hydrocarbons and H_2O in oxygen-deficient zones as such superadiabatic flame temperatures are common for fuel-rich premixed flames.[51−53]

4.2. Gas Composition and Air Entrainment. Figure 3 shows simulated oxygen mass fraction profiles for the flames of Figure 2 that maintain a gas-to-liquid mass ratio (GLMR) of 1.8 (flames 16/20, 32/40, and 64/80). The 16/80 flame is shown as well (GLMR = 7.3; Figure 3d). Flames with GLMR = 1.8 have an initial equivalence ratio (calculated as the mass ratio of supplied fuel to oxygen divided by the ratio for stoichiometric

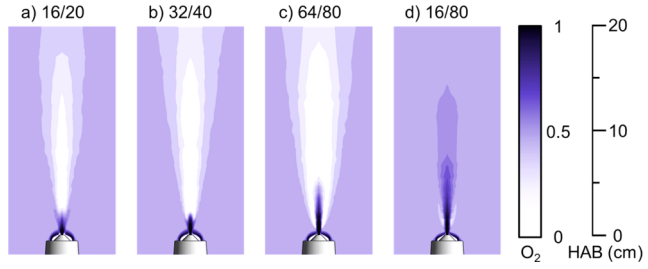

Figure 3. Computed oxygen mass fractions in flames scaled by maintaining a constant GLMR of 1.8 through simultaneously increasing precursor and dispersion O_2 flows from (a) 16/20 to (b) 32/40 and (c) 64/80. Also shown (d) is the 16/80 flame with GLMR = 7.3. Flames with GLMR = 1.8 have a similar oxygen concentration map with an oxygen-depleted center region despite scale-up by four. When the dispersion O_2 flow is increased to GLMR = 7.3, sufficient oxygen is provided for fuel combustion.

combustion) of Φ = 1.2 and thus are fuel-rich, while the flame with GLMR = 7.3 is fuel-lean with Φ = 0.3.

In the largest flame (64/80; Figure 3c), the supplied O_2 dispersion gas (that is intensely mixed with the fuel droplets similar to premixed combustion) is fully depleted already at 0.5 cm HAB along the flame boundaries and by 6 cm at the centerline (white contours). This results in an oxygen-deficient region which extends up to HAB = 20 cm and may explain[51] the measured superadiabatic flame temperatures (Figure 2). Combustion in this region relies on the O_2 entrained from the coflowing air (see Figure 4) that first increases the oxygen concentration in the outer flame regions and then at the centerline. Similar, although narrower and slightly shorter oxygen-free zones are observed for the smaller flames of this GLMR (Figure 3a,b). When the GLMR is increased and the equivalence ratio decreased below unity (16/80 flame, Figure 3d, and 32/80, not shown) the oxygen concentration inside the flame is higher than that in the surrounding air, preventing the formation of oxygen-free regions.

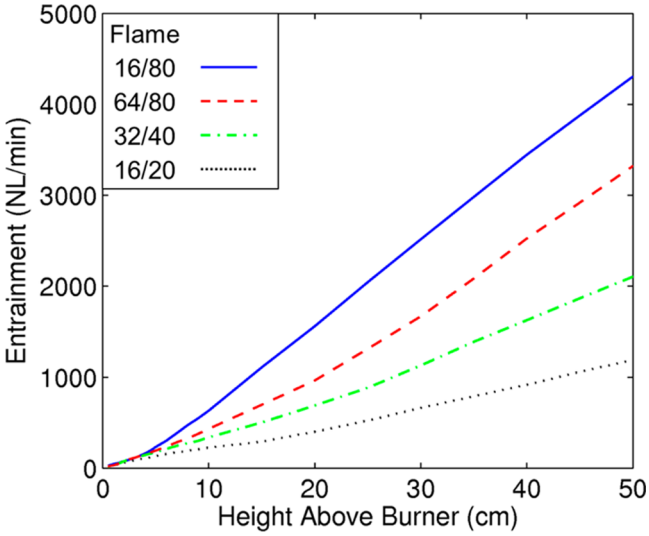

Figure 4. Calculated cumulative air entrainment between HAB = 0–50 cm for spray combustion of 16 (dotted line), 32 (dash-dotted line), or 64 mL/min (dashed line) of precursor solution dispersed by 20, 40, or 80 L/min of O_2, respectively. Also shown is the 16/80 flame (solid line). Dispersion O_2 increases and precursor flow decreases the entrainment rate.

dx.doi.org/10.1021/ie501709s | *Ind. Eng. Chem. Res.* 2014, 53, 10734−10742

Figure 4 shows the cumulative air entrainment of Figure 2 flames as a function of HAB. The entrainment at each HAB was computed as the flow through a velocity isosurface (2 m/s) enclosing the jet (see Figure 1b, cyan contour). For all flame conditions the total entrained flow increased rather linearly with HAB up to 50 cm. The highest entrainment rate of cumulated 4310 L/min at HAB = 50 cm, which corresponds to approximately half of the supplied coflow air, was observed for the 16/80 flame (solid line), consistent with the lowest maximum temperature and steepest cooling gradient (Figure 2, diamonds). Increasing the precursor flow to 64 mL/min increased the maximum temperature (Figure 2, circles) but reduced the total entrainment at HAB = 50 cm to 3320 L/min (dashed line). This is attributed to higher heat release and volumetric gas expansion that has been reported to decrease the entrainment rate.[54,55] Reducing the dispersion O_2 from 80 to 20 L/min along with the precursor flow (64 to 16 mL/min) resulted in lower initial momentum flux which further decreased the total entrainment at HAB = 50 cm to 1190 L/min (dotted line).

4.3. Reactant Conversion and Product Yield. Gas-phase mass fractions of xylenes and zirconium 2-ethylhexanoate (Zr-EHA) normalized by their maximum values are shown in Figure 5 for the 64/80 flame (Figure 3c). Also shown are the

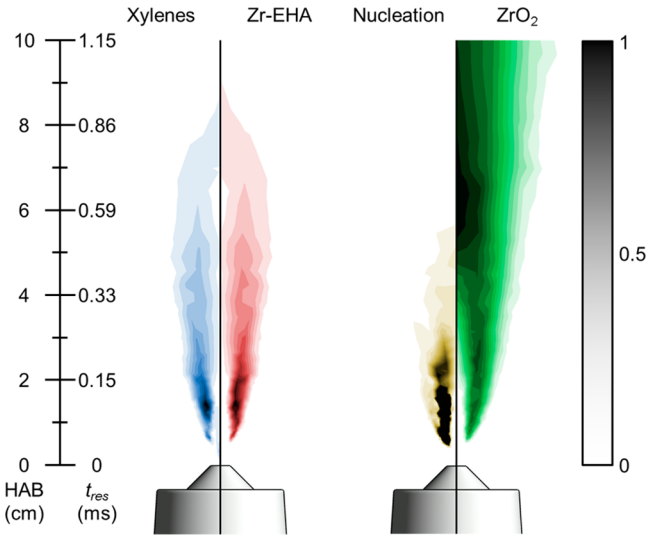

Figure 5. Predicted normalized gas-phase mass fractions of xylenes (blue) and zirconium 2-ethylhexanoate (red) for spray combustion of 64 mL/min of precursor dispersed by 80 L/min of O_2. The ZrO_2 formation profile (brown) and volume concentration (green) are shown as well. Solvent and organometallic precursor evaporate simultaneously up to 9 cm HAB. Nucleation sets in shortly after precursor evaporation slightly off-center and is 95% completed by 3 cm HAB.

ZrO_2 volume concentration and mass nucleation rate normalized with 10% of its maximum for better illustration. Evaporation of xylenes and Zr-EHA proceeds almost simultaneously between 0.5 and 9 cm HAB as is shown by the practically overlapping gas-phase concentration maps. This is attributed to the similar boiling points of xylenes and Zr-EHA, 409 and 460 K, respectively. In contrast, a precursor mixture of ethanol, 1-propanol, and zirconium(IV) *n*-propoxide with respective boiling points of 351, 370, and 481 K showed sequential species evaporation.[18] The combustion of most of the fuel by HAB ~8−9 cm (within 1 ms) coincides with the simulated maximum temperature (see Figure 2, circles).

The nucleation map shows that zirconia formation starts with Zr-EHA evaporation off the center flame axis at about HAB = 0.5 cm and is ~95% completed at ~3−4 cm (light brown legend). Particle formation continues, up to HAB = 9 cm, as Zr-EHA oxidation still takes place. However, its nucleation (ZrO_2 formation) rate is two orders of magnitude lower and therefore not displayed in Figure 5. Up to 4 cm HAB, the highest ZrO_2 mass concentration is off-center (dark green), in agreement with the nucleation map, but shifts to the centerline at larger heights by gas mixing and particle formation. Spreading of the jet flame by air entrainment lowers the particle concentration at the fringes. By HAB = 10 cm, the ZrO_2 particles have dispersed 2 cm away from the centerline.

4.4. Nanoparticle Formation and Growth. Figure 6 shows the product ZrO_2 Sauter mean primary particle diameter (d_p) as a function of precursor flow at constant 80 L/min dispersion O_2 (black triangles and solid line) and at constant GLMR = 1.8 (blue circles and dashed line). Increasing the precursor flow from 16 to 64 mL/min (and the production rate from 118 to 472 g/h) while keeping dispersion O_2 at 80 L/min increased the primary particle size rather linearly from about 8 to 17 nm (triangles) as measured by N_2 adsorption and in good agreement with simulations. Note that the present 3-D model could predict measured average primary particle diameters within 15% consistent with a similar 2-D model performance for laboratory-scale FSP.[18] The particle size increase is consistent with Mueller et al.[13] who reported primary particle growth from about 5 to 31 nm when the ZrO_2 production rate was increased from 50 to 600 g/h by the flow of the 1 M zirconium(IV) *n*-propoxide/ethanol precursor at 50 L/min dispersion O_2.

Now, increasing the dispersion O_2 from 20 to 80 L/min along with the precursor flow (circles) and maintaining a

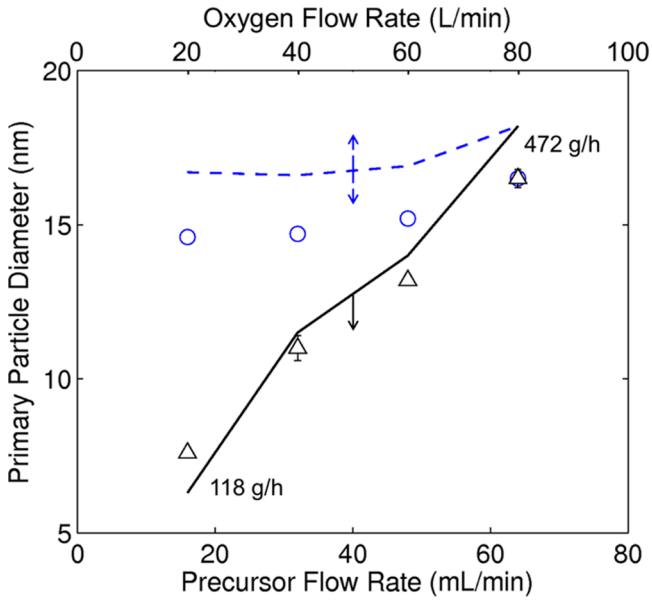

Figure 6. Effect of precursor flow rate on predicted (lines) and measured (symbols) primary particle diameters at constant 80 L/min O_2 dispersion gas (black triangles and solid line) and at constant GLMR = 1.8 (blue circles and dashed line). Similar primary particle size is attained when the precursor to dispersion gas ratio is kept constant during scale-up.

dx.doi.org/10.1021/ie501709s | Ind. Eng. Chem. Res. 2014, 53, 10734−10742

GLMR of 1.8 results in nearly constant primary particle size for both measurements (14.6−16.5 nm) and simulations (16.7−18.2 nm). Again, measured primary particle diameters could be predicted within 15%, which is the difference between monodisperse and polydisperse aerosol dynamics.[45] This shows that the findings of Mädler et al.[20] for constant GLMR scaling in lab-scale ceria synthesis at 2−10 g/h can be extended to 50 times higher production rates and used as a scale-up guide for flame spray synthesis of nanoparticles.

4.5. High-Temperature Particle Residence Time. The present model can elucidate FSP particle dynamics as with the effects of precursor and dispersion O_2 flow rates on particle formation and growth. This is accomplished with the average temperature residence time profiles shown in Figure 7a for

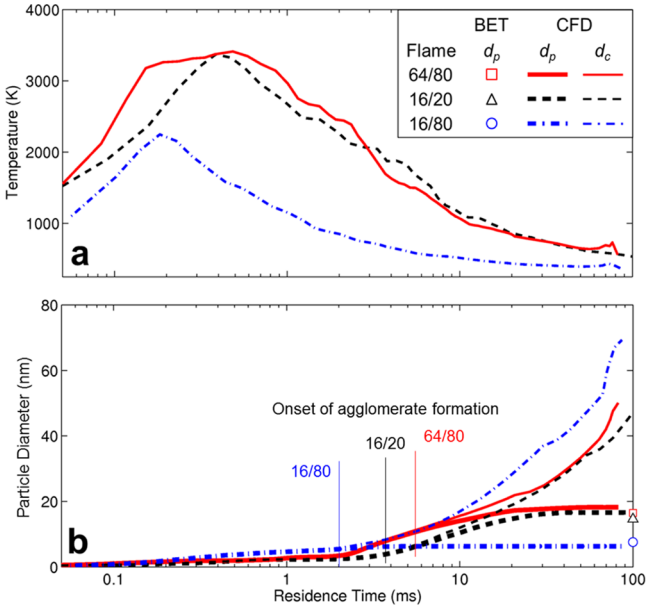

Figure 7. Residence time profiles of the (a) average temperature and (b) Sauter mean primary particle (d_p, thick lines) and agglomerate collision (d_c, thin lines) diameters for the 64/80 (lines), 16/20 (dashed lines), and 16/80 (dash-dotted lines) flames. Also shown are BET-equivalent product particle diameters (symbols) and the beginning of agglomerate formation (vertical lines). Particles made in flames with the same precursor/dispersion O_2 ratio have similar temperature residence time histories and similar primary particle and agglomerate growth profiles.

particles made in flames 64/80 (solid line), 16/20 (dashed line), and 16/80 (dash-dotted line). The temperature residence times at each HAB are radial averages weighed by the ZrO_2 molar concentration to represent profiles for an average ZrO_2 particle, similar to classic cup-mixing averages.[56] Slight differences between the temperatures of Figure 2 and those in Figure 7 are attributed to the different weighing and the presence of Zr-EHA precursor here.

So at 80 L/min dispersion O_2 when the precursor flow is increased from 16 (dash-dotted line) to 64 (solid line) mL/min, the particles experience up to ∼2000 K higher temperature in the first 10 ms while the attainment of the maximum temperature is delayed from ∼0.2 to 0.5 ms, resulting in the observed increase in primary particle diameter from 8 to 17 nm (triangles in Figure 6). When the GLMR, however, is constant at 1.8 during scale-up from 16/20 to 64/80, similar high-temperature residence time histories are obtained leading to similar primary particle diameters (circles in Figure 6) even though the ZrO_2 production rate is increased by a factor of four. The flame with 80 L/min of oxygen (solid line) attains the maximum temperature slightly faster than that with 20 L/min (dashed line). This is attributed to faster reaction by enhanced mixing early in the process indicated by O_2 depletion beginning at lower HAB for increasing production rate at constant GLMR (Figure 3a,c).

Increasing the precursor flow prolongs the high-temperature particle residence time (HTPRT) because the added fuel requires more O_2 for combustion, resulting in longer flames. In addition, chemical reactions may be delayed by the larger size of the O_2-deficient region (Figure 3). Higher dispersion O_2 flows increase the spray flame velocity and reduce the flame temperature through enhanced entrainment of the surrounding cold air (Figure 4). Furthermore, the resulting increased oxygen mass fraction in the spray accelerates fuel consumption (Figure 3).

Figure 7b shows the evolution of the mixing-cup average Sauter mean primary particle (d_p, thick lines) and agglomerate collision diameters (d_c, thin lines) as a function of residence time. Flames with similar HTPRT profiles like 64/80 and 16/20 (Figure 7a) also exhibit similar evolution of product diameters. Primary particles in the 64/80 flame grow initially faster than those in the 16/20 flame as the former results in higher particle concentrations. Specifically, the 64/80 flame had a three times higher maximum particle number concentration, $\sim 2 \times 10^{15}$ versus 7×10^{14} #/cm^3. Product primary particles from the 64/80 flame, however, are only slightly (∼10%) larger than those of the 16/20 flame since sintering limits their further growth. As ZrO_2 sintering is determined by the temperature history, similar primary particles are made by both 64/80 and 16/20 flames.

For the colder flame (16/80), particle formation and subsequent growth takes place faster than in the hotter 64/80 and 16/20 flames but ceases quickly as particles experience rather low temperatures. For all three conditions, most of the particle growth takes place during cooling of the flames (1−100 ms) after chemical reactions are completed (0.1−1 ms, Figure 5). Product primary particle diameters are attained as soon as t = 50 ms and in good agreement with measurements (symbols), as discussed already with Figure 6.

The evolution of the agglomerate collision diameter d_c (Figure 7b, thin lines) mirrors that of the d_p (Figure 7b, thick lines). When the ratio of precursor to dispersion O_2 flow is kept constant during scale-up (thin dashed and solid lines for the 16/20 and 64/80 flames, respectively), agglomerate collision diameters are similar. In contrast, more fractal-like ramified agglomerates with larger collision diameter are formed in the colder flame where the primary particle diameter is smaller (16/80; thin dash-dotted line). Formation of larger agglomerates and smaller primary particles with increased cooling rate is consistent with Heine and Pratsinis[57] investigating silica formation by gas phase hydrolysis of $SiCl_4$ at high concentrations.

4.6. Extent of Hard-Agglomeration (Aggregation). In the early FSP stages where high temperatures prevail and rather small particles are formed, these particles are fully coalesced. Formation of agglomerates ($d_c/d_p > 1$), indicated by the thin vertical lines in Figure 7b, is initiated at ∼2 ms for the 16/80 flame (dash-dotted line). In flames with the same GLMR (16/20 and 64/80), agglomerates start to form after 3 ms. Hard-agglomerates or aggregates (particles held together by sinter

dx.doi.org/10.1021/ie501709s | Ind. Eng. Chem. Res. 2014, 53, 10734−10742

necks) are formed when both d_p and d_c grow. Here this is the case for the hotter flames (64/80 and 16/20). In contrast, for the colder flame 16/80, the d_p hardly grows after the onset of agglomerate formation. This indicates synthesis of soft-agglomerates (particles held together by physical forces) with rather little necking. These smaller particles fully coalesce at lower temperature than larger ones, facilitating formation of soft-agglomerates consisting of loosely attached primary particles. This is in agreement with Eggersdorfer et al.[58] (see Figure 7a there) who observed in laboratory-scale FSP that increasing dispersion O_2 flow rate decreased primary particle diameter and increased formation of agglomerates.

The end of aggregation and the beginning of soft-agglomeration is defined at the height where d_p has reached either 95%[41] or 99%[59] of its final value as sintering ceases. This is the case at approximately 900 K, independent of flame conditions. The ratio d_c/d_p at the corresponding HAB range can quantify the extent of aggregation. For the 16/80 flame, d_c/d_p = 1.16 (95%) or 1.43 (99%) indicating a low degree of aggregation. Product powders should be mostly soft-agglomerates consisting of rather spherical primary particles. Slightly more aggregated particles should be obtained from the 64/80 flame where d_c/d_p = 1.27 (95%) or 1.68 (99%), while for the 16/20 flame d_c/d_p = 1.40 (95%) or 1.66 (99%), suggesting comparable or slightly stronger necking between the primary particles. Therefore, increasing dispersion O_2 during FSP may yield more spherical primary particles as with increasing production rate at constant precursor to dispersion O_2 flow ratio. In both cases, flame dilution by entrainment of the surrounding air is enhanced (Figure 4). This decreases the particle concentration and increases the cooling rate.

Figure 8 shows the scattering intensity of particles made in the 16/20 (dashed line), 64/80 (solid line), and 16/80 (dash-dotted line) flames from SAXS as a function of the scattering vector q. For the smooth surface of primary particles in the Porod regime (q ~0.1 Å^{-1}) the scattered intensity follows a power law decay of the type q^{-4}, i.e., the expected Porod behavior for colloidal objects with sharp interfaces. At smaller q-values, power law exponents are related to the mass-fractal dimension D_f. A unified fit method extending to q-values in the Guinier regime[24,25] yields for the agglomerates fractal dimensions of 2.0 ± 0.2, 2.02 ± 0.02, and 1.79 ± 0.01 for the 16/20, 64/80, and 16/80 flames, respectively. The fractal dimension of ~1.8 for the 16/80 flame is consistent with the expected value for diffusion-limited cluster−cluster agglomerates where primary particles are in point-contact.[60] The measured higher D_f of ~2 for the 16/20 and 64/80 flames indicates that sintering necks have formed between the primary particles[61] in agreement with the predicted stronger aggregation (Figure 7).

Inserts in Figure 8 show TEM micrographs of the filter-collected ZrO_2 particles from the 16/20, 64/80, and 16/80 flames (118−472 g/h ZrO_2 production rate). The 16/80 flame produces primary particles smaller than those of the 16/20 and 64/80 flames consistent with specific surface area measurements (Figure 6). Primary particles are mostly spherical with only few joined together by sintering necks in agreement with the predicted low degree of hard-aggregation (d_c/d_p < 2; Figure 7). The filter collection produces densely packed soft-agglomerates that are difficult to disperse, not providing information on the extent of aggregation.

Figure 9 shows the effect of dispersion gas (black triangles) and constant GLMR = 1.8 scaling (blue circles) on the product

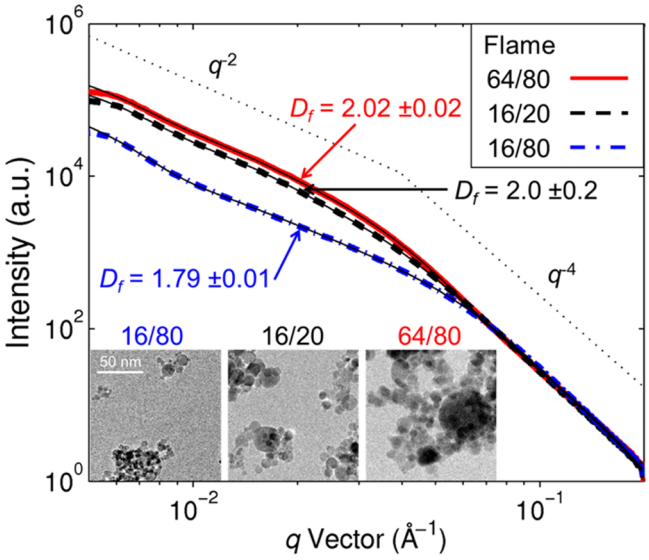

Figure 8. Scattering spectra of the filter-collected product particles made in the 16/20 (dashed line), 64/80 (solid line), and 16/80 (dash-dotted line) flames. In the Porod regime, scattering intensity for all flame conditions follows a power law with exponent −4. The mass fractal dimensions were obtained from the power law by the unified fit theory[25] extending down to the Guinier regime (thin solid lines). The particles from the 16/80 flame show smaller fractal dimension, indicating less sintering or coalescence than those from the 16/20 and 64/80 flames. The inserts are TEM images of the filter-collected and redispersed product particles. The primary particle size for the 16/80 flame is clearly smaller than that for the 16/20 and 64/80 flames, in agreement with nitrogen adsorption data.

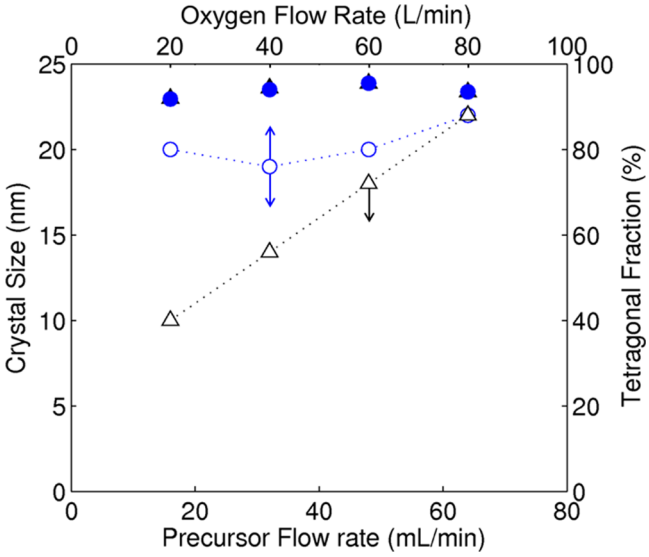

Figure 9. Product ZrO_2 tetragonal phase fraction (right axis, solid symbols) and crystal size (left axis, open symbols) as a function of precursor flow at constant 80 L/min O_2 (triangles) and constant precursor to dispersion O_2 flow ratio (GLMR = 1.8) (circles). Also, the product crystallinity is maintained during constant GLMR scaling.

powder crystallinity. The tetragonal phase fraction of all powders is 92−96 wt % (right axis, filled symbols) with the balance being monoclinic. The tetragonal crystal size (open symbols) increases from 10 to 22 nm with increasing precursor flow at 80 L/min O_2 while it stays constant at 20.5 ± 1.5 nm for constant GLMR, following the trends of the primary particle

dx.doi.org/10.1021/ie501709s | Ind. Eng. Chem. Res. 2014, 53, 10734−10742

size (Figure 6) and showing that also the particle crystallinity is maintained during constant GLMR scaling. For all FSP conditions, the tetragonal crystal size is ∼4 nm larger than the primary particle diameter (Figure 6). This suggests that the particles are mostly monocrystalline while the shift to larger sizes is due to the different averages from XRD and BET (volume versus surface, respectively). The average size of the monoclinic crystals is 25−49 nm and significantly larger than the average primary particle diameter. This size range is similar to that of the individual large particles in the product powder (TEM images in Figure 8). These particles may represent the large tail of the particle size distribution or might have experienced much longer high-temperature residence times or a different formation mechanism, i.e., direct formation from large droplets that were not well-atomized or escaped the flame.

5. CONCLUSIONS

In scale-up of nanoparticle production by flame spray pyrolysis (FSP) from ∼100 to 500 g/h of zirconia, the product primary particle and agglomerate size as well as the crystallinity are conserved when the precursor and the dispersion flow are increased by the same factor, keeping the gas-to-liquid mass ratio constant. This is attributed to similar high-temperature particle residence times revealed by process simulation with a CFD-based model employing transport-limited precursor oxidation and monodisperse particle dynamics. This simple and robust model, which accounts for the detailed 3-dimensional reactor geometry and requires neither experimental input data such as temperature or velocity measurements nor empirical correlations for boundary conditions, predicted the measured product primary particle diameters with 15% accuracy, which is within the difference between monodisperse and polydisperse aerosol dynamics. Increasing the precursor feed and production rate while keeping the dispersion gas flow constant prolongs the HTPRT, resulting in larger, more aggregated primary particles because of increased flame enthalpy and lower air entrainment rates as well as the formation of oxygen-deficient flame regions. The process simulation helps to identify such oxygen as well as entrainment requirements and can guide the selection of appropriate operation conditions. Accounting for complete and detailed reactor geometry enables employing the model for parametric studies of different nozzle and reactor chamber designs.

■ ASSOCIATED CONTENT

Supporting Information

Detailed description of the employed CFD model. This material is available free of charge via the Internet at http://pubs.acs.org.

■ AUTHOR INFORMATION

Corresponding Author

*Tel: +41-44-632-2503. Fax: +41-44-632-1595. E-mail: wegner@ptl.mavt.ethz.ch.

Notes

The authors declare no competing financial interest.

■ ACKNOWLEDGMENTS

The research leading to these results has received funding from the European Community's Seventh Framework Programme (FP7/2007-2013) under Grant Agreement 228885, the European Research Council (FP7/2007−2013)/ERC under Grant Agreement 247283, and the Swiss National Science Foundation R'Equip Grant 206021-121359/1. We gratefully acknowledge the support of Dr. F. Krumeich for TEM imaging.

■ REFERENCES

(1) Roth, P. Particle Synthesis in Flames. *Proc. Combust. Inst.* **2007**, *31*, 1773.
(2) Ulrich, G. D. Flame Synthesis of Fine Particles. *Chem. Eng. News* **1984**, *62*, 22.
(3) Wegner, K.; Pratsinis, S. E. Scale-up of Nanoparticle Synthesis in Diffusion Flame Reactors. *Chem. Eng. Sci.* **2003**, *58*, 4581.
(4) Sokolowski, M.; Sokolowska, A.; Michalski, A.; Gokieli, B. The "In-Flame-Reaction" Method for Al_2O_3 Aerosol Formation. *J. Aerosol Sci.* **1977**, *8*, 219.
(5) Pratsinis, S. E. Aerosol-Based Technologies in Nanoscale Manufacturing: From Functional Materials to Devices through Core Chemical Engineering. *AIChE J.* **2010**, *56*, 3028.
(6) Grass, R. N.; Athanassiou, E. K.; Stark, W. J. Covalently Functionalized Cobalt Nanoparticles as a Platform for Magnetic Separations in Organic Synthesis. *Angew. Chem., Int. Ed.* **2007**, *46*, 4909.
(7) TurboBeads. http://www.turbobeads.com/ (accessed 10.06.2014).
(8) Wegner, K.; Schimmoeller, B.; Thiebaut, B.; Fernandez, C.; Rao, T. Pilot Plants for Industrial Nanoparticle Production by Flame Spray Pyrolysis. *KONA Powder Part. J.* **2011**, *29*, 251.
(9) Pratsinis, S. E. Aerosol-Based Technologies in Nanoscale Manufacturing: From Functional Materials to Devices through Core Chemical Engineering. *AIChE J.* **2010**, *56*, 3028.
(10) Strobel, R.; Pratsinis, S. E. Flame Aerosol Synthesis of Smart Nanostructured Materials. *J. Mater. Chem.* **2007**, *17*, 4743.
(11) Laine, R.; Hinklin, T.; Williams, G.; Rand, S. Low-Cost Nanopowders for Phosphor and Laser Applications by Flame Spray Pyrolysis. *J. Metastable Nanocryst. Mater.* **2000**, *8*, 500.
(12) Mueller, R.; Mädler, L.; Pratsinis, S. E. Nanoparticle Synthesis at High Production Rates by Flame Spray Pyrolysis. *Chem. Eng. Sci.* **2003**, *58*, 1969.
(13) Mueller, R.; Jossen, R.; Pratsinis, S. E.; Watson, M.; Akhtar, M. K. Zirconia Nanoparticles Made in Spray Flames at High Production Rates. *J. Am. Ceram. Soc.* **2004**, *87*, 197.
(14) Jossen, R.; Mueller, R.; Pratsinis, S. E.; Watson, M.; Akhtar, M. K. Morphology and Composition of Spray-Flame-Made Yttria-Stabilized Zirconia Nanoparticles. *Nanotechnology* **2005**, *16*, S609.
(15) Heel, A.; Holtappels, P.; Hug, P.; Graule, T. Flame Spray Synthesis of Nanoscale $La_{0.6}Sr_{0.4}Co_{0.2}Fe_{0.8}O_{3-\delta}$ and $Ba_{0.5}Sr_{0.5}Co_{0.8}Fe_{0.2}O_{3-\delta}$ as Cathode Materials for Intermediate Temperature Solid Oxide Fuel Cells. *Fuel Cells* **2010**, *10*, 419.
(16) Hembram, K.; Sivaprakasam, D.; Rao, T.; Wegner, K. Large-Scale Manufacture of ZnO Nanorods by Flame Spray Pyrolysis. *J. Nanopart. Res.* **2013**, *15*, 1.
(17) Pratsinis, S. E. Flame Aerosol Synthesis of Ceramic Powders. *Prog. Energy Combust. Sci.* **1998**, *24*, 197.
(18) Gröhn, A. J.; Pratsinis, S. E.; Wegner, K. Fluid-Particle Dynamics During Combustion Spray Aerosol Synthesis of ZrO_2. *Chem. Eng. J.* **2012**, *191*, 491.
(19) Sadakata, M.; Xu, Y. B.; Harano, A. A Systematic Approach for the Design of Aerosol Reactors. *Powder Technol.* **1996**, *88*, 261.
(20) Mädler, L.; Stark, W. J.; Pratsinis, S. E. Flame-Made Ceria Nanoparticles. *J. Mater. Res.* **2002**, *17*, 1356.
(21) Wegner, K.; Pratsinis, S. E. Gas-Phase Synthesis of Nanoparticles: Scale-up and Design of Flame Reactors. *Powder Technol.* **2005**, *150*, 117.
(22) Heine, M. C.; Mädler, L.; Jossen, R.; Pratsinis, S. E. Direct Measurement of Entrainment during Nanoparticle Synthesis in Spray Flames. *Combust. Flame* **2006**, *144*, 809.
(23) Whitney, E. D. *Ceramic Cutting Tools: Materials, Development and Performance*; William Andrew Publishing: New Jersey, 1994.

(24) Beaucage, G. Approximations Leading to a Unified Exponential/Power-Law Approach to Small-Angle Scattering. *J. Appl. Crystallogr.* **1995**, *28*, 717.
(25) Beaucage, G. Small-Angle Scattering from Polymeric Mass Fractals of Arbitrary Mass-Fractal Dimension. *J. Appl. Crystallogr.* **1996**, *29*, 134.
(26) Prosen, E.; Gilmont, R.; Rossini, F. Heats of Combustion of Benzene, Toluene, Ethyl-Benzene, *o*-Xylene, *m*-Xylene, *p*-Xylene, *n*-Propylbenzene, and Styrene. *J. Res. Natl. Bur. Stand.* **1945**, *34*, 65.
(27) Stridh, G. Enthalpy of Formation of 2-Ethylhexanoic Acid. *Zh. Khim. Termodin. Termokhim.* **1976**, *8*, 193.
(28) Morrison, P. W.; Raghavan, R.; Timpone, A. J.; Artelt, C. P.; Pratsinis, S. E. In Situ Fourier Transform Infrared Characterization of the Effect of Electrical Fields on the Flame Synthesis of TiO_2 Particles. *Chem. Mater.* **1997**, *9*, 2702.
(29) Kammler, H. K.; Pratsinis, S. E.; Morrison, P. W.; Hemmerling, B. Flame, Temperature Measurements During Electrically Assisted Aerosol Synthesis of Nanoparticles. *Combust. Flame* **2002**, *128*, 369.
(30) Ansys, *Ansys Fluent 12.0 Theory Guide*; ANSYS, Inc.: Canonsburg, PA, 2009; v.12.0.1.
(31) Shih, T. H.; Liou, W. W.; Shabbir, A.; Yang, Z. G.; Zhu, J. A New κ-ε Eddy Viscosity Model for High Reynolds Number Turbulent Flows. *Comput. Fluids* **1995**, *24*, 227.
(32) Patankar, S. V. *Numerical Heat Transfer and Fluid Flow*; Hemisphere Publishing Company: New York, 1980.
(33) Reitz, R. D.; Diwakar, R. Structure of High-Pressure Fuel Sprays. *SAE Tech. Pap. Ser.* **1987**, DOI: 10.4271/870598.
(34) Reitz, R. D. Modeling Atomization Processes in High-Pressure Vaporizing Sprays. *Atomisation Spray Technol.* **1987**, *3*, 309.
(35) Habchi, C.; Verhoeven, D.; Huu, C. H.; Lambert, L.; Vanhemelryck, J.; Baritaud, T. Modeling Atomization and Break up in High-Pressure Diesel Sprays. *SAE Trans.* **1997**, *106*, 1391.
(36) Pilch, M.; Erdman, C. Use of Breakup Time Data and Velocity History Data to Predict the Maximum Size of Stable Fragments for Acceleration-Induced Breakup of a Liquid Drop. *Int. J. Multiphase Flow* **1987**, *13*, 741.
(37) Liu, A. B.; Mather, D.; Reitz, R. D. *Modeling the Effects of Drop Drag and Breakup on Fuel Sprays*; SAE Technical Paper 930072, 1993.
(38) Magnussen, B. F.; Hjertager, B. H. On Mathematical Modelling of Turbulent Combustion with Special Emphasis on Soot Formation and Combustion. *Symp. (Int.) Combust. [Proc.]* **1977**, *16*, 719.
(39) Westbrook, C. K.; Dryer, F. L. Simplified Reaction-Mechanisms for the Oxidation of Hydrocarbon Fuels in Flames. *Combust. Sci. Technol.* **1981**, *27*, 31.
(40) Satterfield, C. N.; Loftus, J. Kinetics of the Homogeneous Partial Oxidation of *o*-Xylene Vapor by Air. *Ind. Eng. Chem. Process Des. Dev.* **1965**, *4*, 102.
(41) Gröhn, A. J.; Buesser, B.; Jokiniemi, J. K.; Pratsinis, S. E. Design of Turbulent Flame Aerosol Reactors by Mixing-Limited Fluid Dynamics. *Ind. Eng. Chem. Res.* **2011**, *50*, 3159.
(42) Kruis, F. E.; Kusters, K. A.; Pratsinis, S. E.; Scarlett, B. A Simple-Model for the Evolution of the Characteristics of Aggregate Particles Undergoing Coagulation and Sintering. *Aerosol Sci. Technol.* **1993**, *19*, 514.
(43) Landgrebe, J. D.; Pratsinis, S. E. Gas-Phase Manufacture of Particulates - Interplay of Chemical-Reaction and Aerosol Coagulation in the Free-Molecular Regime. *Ind. Eng. Chem. Res.* **1989**, *28*, 1474.
(44) Mueller, R.; Jossen, R.; Kammler, H. K.; Pratsinis, S. E. Growth of Zirconia Particles Made by Flame Spray Pyrolysis. *AIChE J.* **2004**, *50*, 3085.
(45) Tsantilis, S.; Kammler, H. K.; Pratsinis, S. E. Population Balance Modeling of Flame Synthesis of Titania Nanoparticles. *Chem. Eng. Sci.* **2002**, *57*, 2139.
(46) Mountain, R. D.; Mulholland, G. W. Light Scattering from Simulated Smoke Agglomerates. *Langmuir* **1988**, *4*, 1321.
(47) Coblenz, W. S.; Dynys, J. M.; Cannon, R. M.; Coble, R. L. Initial Stage Solid State Sintering Models. A Critical Analysis and Assessment. *Mater. Sci. Res.* **1980**, *13*, 141.
(48) Brossmann, U.; Wurschum, R.; Sodervall, U.; Schaefer, H. E. Oxygen Diffusion in Ultrafine Grained Monoclinic ZrO_2. *J. Appl. Phys.* **1999**, *85*, 7646.
(49) Christensen, A.; Carter, E. A. First-Principles Study of the Surfaces of Zirconia. *Phys. Rev. B* **1998**, *58*, 8050.
(50) Mädler, L.; Kammler, H. K.; Mueller, R.; Pratsinis, S. E. Controlled Synthesis of Nanostructured Particles by Flame Spray Pyrolysis. *J. Aerosol Sci.* **2002**, *33*, 369.
(51) Liu, F.; Guo, H.; Smallwood, G. J.; Gülder, Ö. L. Numerical Study of the Superadiabatic Flame Temperature Phenomenon in Hydrocarbon Premixed Flames. *Proc. Combust. Inst.* **2002**, *29*, 1543.
(52) Kattaa, V. R.; Meyer, T. R.; Gord, J. R.; Roquemore, W. M. Insights into Non-Adiabatic-Equilibrium Flame Temperatures during Millimeter-Size Vortex/Flame Interactions. *Combust. Flame* **2003**, *132*, 639.
(53) Park, J.; Kwon, O. B.; Yun, J. H.; Keel, S. I.; Chang Cho, H.; Kim, S. Preferential Diffusion Effects on Flame Characteristics in H_2/CO Syngas Diffusion Flames Diluted with CO_2. *Int. J. Hydrogen Energy* **2008**, *33*, 7286.
(54) Ricou, F. P.; Spalding, D. B. Measurements of Entrainment by Axisymmetrical Turbulent Jets. *J. Fluid Mech.* **1961**, *11*, 21.
(55) Muniz, L.; Mungal, M. G. Effects of Heat Release and Buoyancy on Flow Structure and Entrainment in Turbulent Nonpremixed Flames. *Combust. Flame* **2001**, *126*, 1402.
(56) Bird, R. B.; Stewart, W. E.; Lightfoot, E. N. *Transport Phenomena*; 2nd ed.; John Wiley & Sons: New York, 2002.
(57) Heine, M.; Pratsinis, S. High Concentration Agglomerate Dynamics at High Temperatures. *Langmuir* **2006**, *22*, 10238.
(58) Eggersdorfer, M. L.; Gröhn, A. J.; Sorensen, C. M.; McMurry, P. H.; Pratsinis, S. E. Mass-Mobility Characterization of Flame-Made ZrO_2 Aerosols: Primary Particle Diameter and Extent of Aggregation. *J. Colloid Interface Sci.* **2012**, *387*, 12.
(59) Tsantilis, S.; Pratsinis, S. E. Soft- and Hard-Agglomerate Aerosols Made at High Temperatures. *Langmuir* **2004**, *20*, 5933.
(60) Jullien, R.; Botet, R. *Aggregation and Fractal Aggregates*; World Scientific Publishing Company, Incorporated: Singapore, 1987.
(61) Eggersdorfer, M. L.; Kadau, D.; Herrmann, H. J.; Pratsinis, S. E. Aggregate Morphology Evolution by Sintering: Number and Diameter of Primary Particles. *J. Aerosol Sci.* **2012**, *46*, 7.